RESEARCH ARTICLE

Journal
& American Ceramic Society

Temperature-dependent mechanical and oxidation behavior of in situ formed ZrN/ZrO$_2$-containing Si$_3$N$_4$-based composite

Jiongjie Liu[1] | Wei Li[1] | Emmanuel Ricohermoso III[1] | Zhuihui Qiao[2] |
Qingwen Dai[3] | Xingmin Liu[1] | Wenjie Xie[1] | Emanuel Ionescu[1,4] |
Anke Weidenkaff[1,4] | Ralf Riedel[1]

[1]Institute of Materials Science, Technical University of Darmstadt, Darmstadt, Germany

[2]State Key Laboratory of Solid Lubrication, Lanzhou Institute of Chemical Physics, Chinese Academy of Sciences, Lanzhou, P. R. China

[3]College of Mechanical and Electrical Engineering, Nanjing University of Aeronautics & Astronautics, Nanjing, China

[4]Department Digitalization of Resources, Fraunhofer IWKS, Alzenau, Germany

Correspondence
Jiongjie Liu, Institute of Materials Science, Technical University of Darmstadt, Darmstadt 64287, Germany.
Email: jiongjieliu92@gmail.com

Funding information
Sino-German (CSC-DAAD) Postdoc Scholarship Program, 2020, Grant/Award Number: 57531629; Deutsche Forschungsgemeinschaft, Grant/Award Number: GRK 2561

Abstract

In this work, Si$_3$N$_4$ and Zr(NO$_3$)$_4$ were used as raw materials to prepare ZrN/ZrO$_2$-containing Si$_3$N$_4$-based ceramic composite. The processing, phase composition, and microstructure of the composite were investigated. Hardness and fracture toughness of the ceramics were evaluated via Vickers indentation in Ar at 25°C, 300°C, 600°C, and 900°C. During spark plasma sintering, Zr(NO$_3$)$_4$ was transformed into tetragonal ZrO$_2$, which further reacted with Si$_3$N$_4$, resulting in the formation of ZrN. The introduction of ZrN enhanced the high-temperature mechanical properties of the composite, and its hardness and fracture toughness reached 13.4 GPa and 6.1 MPa·m$^{1/2}$ at 900°C, respectively. The oxidation experiment was carried out in air at 1000°C, 1300°C, and 1500°C for 5 h. It was shown that high-temperature oxidation promoted the formation and growth of porous oxide layers. The microstructure and phase composition of the formed oxide layers were investigated in detail. Finally, it was identified that the obtained composite exhibited a higher thermal diffusivity than that of monolithic Si$_3$N$_4$ in the temperature range of 100°C–1000°C.

KEYWORDS
mechanical properties, oxidation, silicon nitride, thermal properties, zirconia

1 | INTRODUCTION

In contrast to metals and polymers, structural ceramics exhibit significant performance advantages, such as low density, high hardness, chemical stability, high temperature, and corrosion resistance.[1–4] Ceramics are thus processed into structural parts, for example, bearings, sealing rings, turbines, and nose cones of aircrafts for service in harsh environments.[5,6] As a typical non-oxide ceramic,

silicon nitride (Si$_3$N$_4$) has attracted extensive attention from academia and industry. It has been shown that the thermal conductivity of Si$_3$N$_4$ can be up to 177 W/(m·K) along with a fracture toughness of 11.2 MPa·m$^{1/2}$ and a fracture strength of 460 MPa.[7,8] In addition, the high covalent character of the Si–N bond determines the resistance against decomposition (≥1800°C in nitrogen) and excellent tribological properties at elevated temperatures.[9,10] Nevertheless, the low tolerance for damage and defect is

still one of the main factors limiting its further industrial development. High operation temperatures as well as oxidative and erosive environmental conditions negatively impact the mechanical strength of Si_3N_4,[11,12] leading to material loss and sudden failure of ceramic parts.[13,14]

In the past few decades, the development of composites has opened new avenues to flexibly access various compositions of ceramics.[15,16] A large number of studies have confirmed that the incorporation of secondary phases not only affects the phase evolution and microstructure of the material but also enhances the strength and toughness compared to that of the monolithic materials.[17,18] Among many additives, zirconium-based compounds (e.g., ZrB_2, ZrC, ZrN, and ZrO_2) are regarded as ideal candidates with remarkable mechanical and high-temperature stability.[19–21] Guo et al.[22] prepared a ZrB_2-containing Si_3N_4-based composite at a low temperature of 1500°C. It was found that the addition of ZrB_2 promoted the phase transition of Si_3N_4 from α to β, and the obtained composite exhibited improved fracture toughness and bending strength of 9.8 MPa·m$^{1/2}$ and 702.0 MPa, respectively. Sayyadi-Shahraki et al.[23] reported dense Si_3N_4/ZrO_2 ceramic composites fabricated via spark plasma sintering (SPS) at 1600°C. It was shown that the introduction of Y_2O_3-stabilized ZrO_2 into Si_3N_4 facilitated densification of ceramic composites during SPS, decreasing the sintering temperature of Si_3N_4 from 1600°C to 1420°C. Furthermore, Talmy et al.[24] characterized the chemical stability and oxidation behavior of Si_3N_4-containing ZrB_2 at 1200°C–1500°C. The results suggested that the formation of a protective layer of borosilicate glass during high-temperature annealing contributed to the significant improvement in the oxidation resistance of the ZrB_2/Si_3N_4 composite.

Although promising, the methods involving processing and preparation of ceramic composites still face practical difficulties, which weaken the final properties of the ceramic composite.[25–27] Traditionally, the secondary phases are added directly to Si_3N_4 matrix through physical mixing (e.g., mechanical stirring and ball milling), which inevitably results in the agglomeration of the additives and thus in the formation of pores and micro-cracks in the ceramic matrices.[28] Along with the temperature transition induced by the heating environment, these micro-cracks are prone to spread under the action of thermal stress, ultimately manifesting as the failure fracture of ceramics.[29] In addition, the mismatch of the thermal expansion coefficient and chemical incompatibility between the individual phases reduces the densification of composites, triggering more defect nucleation and insufficient mechanical properties.[30,31] In our previous study,[32,33] it was determined that the in situ generation of the secondary phases is an effective way to reduce the structural defects caused by particle agglomeration. Typically, Ag-containing Si_3N_4-based composites were successfully produced by using

$AgNO_3$ as a metal precursor. The results demonstrated that the in situ formed Ag particles with a size of ~1 μm were evenly dispersed in the grain boundary of Si_3N_4, and the resulting ceramics displayed improved toughness and tribological properties relative to pure Si_3N_4.

In this work, a Zr-containing Si_3N_4-based ceramic composite was successfully prepared via the SPS process using Si_3N_4 and $Zr(NO_3)_4$ as the raw materials. The phase composition and microstructure of the composite were investigated. By the introduction of the Vickers indentation at elevated temperatures of 25°C, 300°C, 600°C, and 900°C in Ar, the hardness of the ceramics was evaluated, and the corresponding fracture toughness was calculated based on the indentation method. Additionally, the Si_3N_4-based composite was oxidized in air at 1000°C, 1300°C, and 1500°C for 5 h. The chemical composition and microstructure of the oxide layers were characterized with temperature, and their effect on the thermal diffusivity of ceramics was analyzed. The main aim of this work is to explore the thermo-mechanical properties of the Zr-containing Si_3N_4 composite and expand its application at high temperatures.

2 | EXPERIMENT

2.1 | Sample preparation

The starting materials used for SPS were composed of 90 wt.% α-Si_3N_4 (99.9%, 0.50–0.75 μm, Anyang JSH New Material Co., Henan, China) and sintering aids of 6 wt.% Y_2O_3 and 4 wt.% Al_2O_3 provided by Lida Hi-Tech Special Material Co., Jiangsu, China (99.9%, 0.5 μm). The powder was mixed for 8 h at 300 rpm in a Teflon tank using a planetary ball mill (QM-3SP4, Nanjing University Instrument Factory, Nanjing, China). The grinding ball consisted of Si_3N_4, and the ball-to-powder ratio was 5:1. The zirconyl nitrate pentahydrate ($Zr(NO_3)_4 \cdot 5H_2O$, Kelong Chemical Reagent Factory, Chengdu, China) as the Zr source was first dissolved in deionized water, followed by addition into pre-mixed powder with a mass fraction of 20 wt.%. The slurry was subsequently stirred at 80°C in a rotary evaporator until the solvent was removed totally. The dried lump was ground, sieved (100 mesh), and then loaded into a graphite die (diameter 25 mm) for SPS (LABOX-3010KF, Japan). Before that, a layer of graphite paper (thickness 0.03 mm) was padded on the inner wall of the die to prevent the powder from sticking. The sintering parameters included a sintering temperature of 1680°C, heating rate of 90°C/min, axial pressure of 30 MPa, holding time of 5 min, and vacuum degree ranging from 10 to 20 Pa. For convenience, the monolithic Si_3N_4 and Zr-containing Si_3N_4-based composite are defined as samples SN and SNZ, respectively.

2.2 | Performance tests

The sintered ceramic discs were polished by an automatic polisher Phoenix 4000. The density of ceramics was measured by the Archimedes' water immersion. The Vickers hardness was obtained using high-temperature hardness tester (HTV-PHS30, Archimedes Industry Technology Co. Ltd., England), in which the applied load was 10 kg and the holding time was 10 s. The test was performed at 25°C, 300°C, 600°C, and 900°C in Ar, and each test was repeated at least 10 times to ensure reliability. After hardness measurement (10 kg), the clear cracks along the indentation corners were produced, and the fracture toughness of the ceramics was calculated based on the indentation method according to reference.[34] The ceramics for the oxidation test were cut into square sizes of 6 mm × 6 mm × 2 mm using the precision surface grinding machine ELB SWH-5 ND. Oxidation proceeded in a muffle furnace at 1000°C, 1300°C, and 1500°C for 5 h. The thermal diffusivity of samples was measured using a laser flash apparatus (LFA 457, NETZSCH, Germany) under the Ar atmosphere with a gas flow rate of 50 mL/min.

2.3 | Characterization

Powder X-ray diffraction (XRD) was performed to analyze the phase composition of the synthesized SN-based composites via XRD diffractometer utilizing Mo $K_{\alpha 1}$ radiation source (STOE & Cie GmbH, Germany), while the samples with oxide layer were analyzed using XRD diffractometer (Bruker D8 Advanced, Germany) with Cu K_{α} radiation. Rietveld refinement of the obtained XRD patterns was performed using the General Structure Analysis Software-II (GSAS-II) software package. The surface morphology of ceramics after oxidation was observed using light microscopy (Zeiss Axio Imager 2, Germany). The microstructure of the cross-section was characterized using scanning electron microscopy (JEOL JSM 7600 F, Japan) equipped with energy-dispersive X-ray spectroscopy (EDS). The oxide films were identified by a Raman spectrometer (Horiba JobinYvon, Bensheim, Germany) with a laser wavelength of 514 nm.

3 | RESULTS AND DISCUSSION

After sintering at 1680°C, Si_3N_4 (sample SN) has been completely transformed from the initial α- to the final β- phase (hexagonal, P63, ref. 01-082-0709) (see Figure S1). For sample SNZ, in addition to the β-Si_3N_4, new crystal phases regarding ZrO_2 (tetragonal, P42/nmc, ref. 00-024-1664) and ZrN (cubic, Fm-3 m, ref. 01-74-1217) are retrieved with the addition of $Zr(NO_3)_4$ (see Figure 1). The diffraction peak of $Zr(NO_3)_4$ is not found in the pattern. This result indicates that during sintering, $Zr(NO_3)_4$ has been completely decomposed, and the decomposition products react with Si_3N_4, resulting in the formation of ZrO_2 and ZrN. The specific reaction process can be found in Equations (1) and (2). After Rietveld refinement, it is confirmed that the amounts of Si_3N_4, ZrO_2, and ZrN are 67.3, 10.7, and 22.0 wt.%, respectively. Compared to 72 wt.% Si_3N_4 before sintering, the mass loss of Si_3N_4 is on the one hand attributed to the reaction with ZrO_2; on the other hand, it may be related to the high-temperature decomposition of Si_3N_4 under vacuum.[35] In addition, it is worth noting that ZrO_2 usually possesses three crystalline phases: monoclinic (m-ZrO_2), tetragonal (t-ZrO_2), and cubic (c-ZrO_2), and the temperature-driven transitions between these phases are often accompanied by a volume change, which is a tricky problem and prevents the applications of ZrO_2 over a broader temperature range.[36] Herein, it is determined that using $Zr(NO_3)_4$ as the precursor, the in situ formed ZrO_2 is a tetragonal phase, and no transition to the monoclinic phase occurs when the sample is free cooled to room temperature. Also, it needs to point out that the graphite peak in the pattern of 26.3° comes from the graphite paper.

$$Zr(NO_3)_{4(s)} = ZrO_{2(s)} + 4NO_{2(g)} + O_{2(g)} \quad (1)$$

$$6ZrO_{2(s)} + 4Si_3N_{4(s)} = 6ZrN_{(s)} + 12SiO_{(g)} + 5N_{2(g)} \quad (2)$$
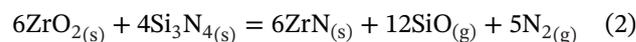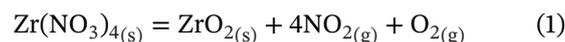
In order to illustrate the advantages of in situ method displayed here, ZrO_2-containing Si_3N_4-based composite as a reference sample is prepared by directly adding ZrO_2 powder into Si_3N_4. The XRD analysis (Figure S1) shows that the resulting composite prepared by this physical mixing and sintering is not conducive to the formation of hard phase ZrN.

Figure 2 displays the sintering curve of samples monitored by the SPS equipment, in which the sintering temperature, axial displacement (the upper electrode is fixed, the lower electrode rises), and pressure in the furnace chamber are recorded in time. Accompanied by the changes in displacement and chamber pressure, the sintering behavior is identified. For monolithic sample SN, the sintering process occurs as expected. As shown in Figure 2a, from $T_1 = 740°C$ to $T_2 = 1555°C$, the displacement curve gradually rises, which corresponds to the densification of the ceramic. At this time, the vacuum degree of the chamber is basically stable. In contrast, for SNZ-based composite, the sintering process is roughly divided into three stages. Stage 1 records that with the increase of temperature, the chamber pressure rises gradually,
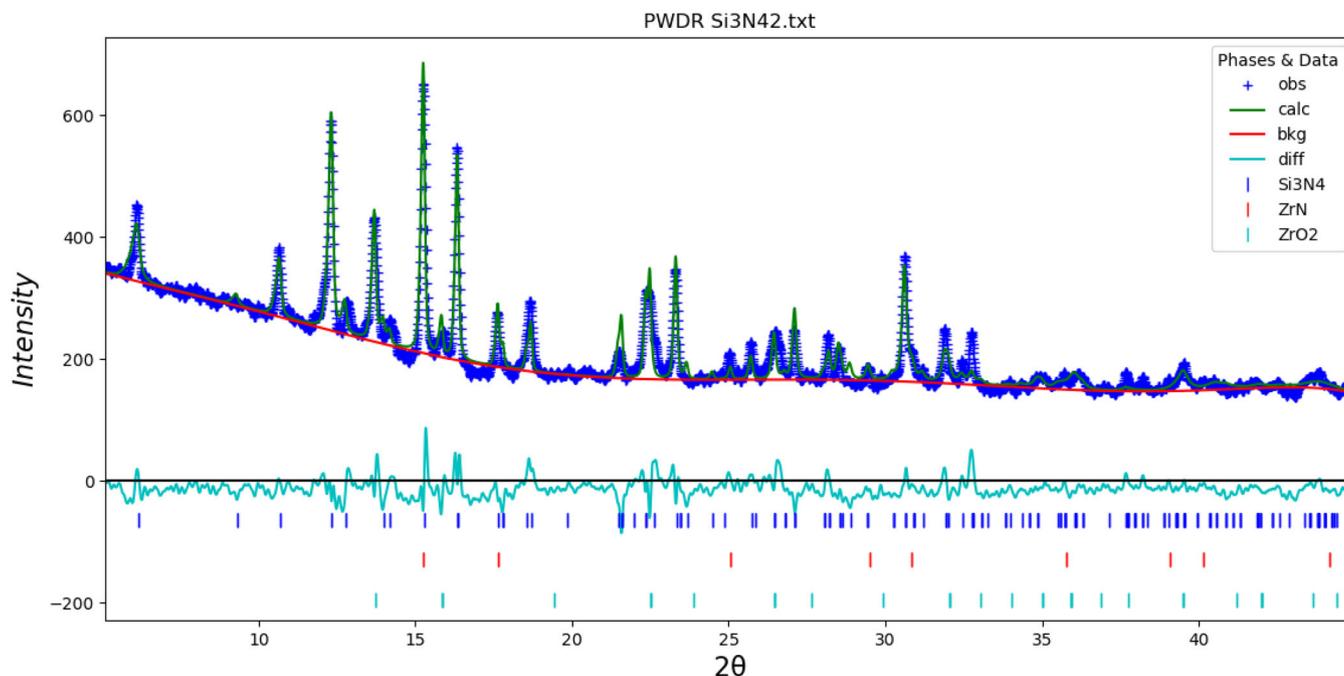
FIGURE 1 X-ray diffraction (XRD) pattern of Zr-containing Si_3N_4-based composite after spark plasma sintering (SPS) at 1680°C.
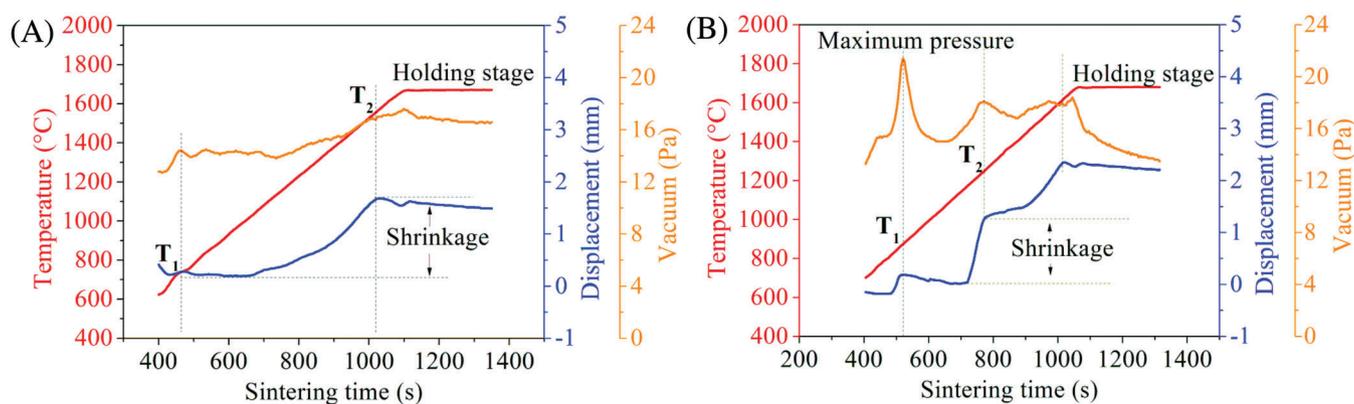
FIGURE 2 Spark plasma sintering (SPS) curves of (a) monolithic Si_3N_4 and (b) Zr-containing Si_3N_4-based composite.

which reaches a maximum at $T_1 = 880°C$, indicating that gas is released continuously, and this may be a result of the desorption of water molecules and the decomposition of $Zr(NO_3)_4$.[37] Stage 2 shows that the displacement curve decreases slightly and then shrinks sharply as the temperature increases to $T_2 = 1250°C$. Correspondingly, the pressure in the chamber climbs again, which is speculated to be relevant to the chemical reactions and densification of the green body. Stage 3 covers that the shrinkage rate of displacement is slowed down, and the chamber pressure tends to be stable, suggesting that the ceramic at this time undergoes further densification.

The microstructure of the Si_3N_4-based composite was studied via backscattered scanning electron microscopy. From Figure 3a, it is seen that a large number of bright particles are evenly dispersed in the dark Si_3N_4 matrix. For more information, local areas are magnified in Figure 3b,c. The corresponding EDS point analysis is carried out. As shown in spectrum 1 (Figure 3d), there is an obvious enrichment of Zr. Combined with XRD results, it can be concluded that these bright particles with a size of ~1 μm are identified as crystalline phases ZrO_2 or ZrN. However, as a semi-quantitative analysis method, it is difficult to differentiate between ZrO_2 and ZrN particles. In addition, according to spectra 2 and 3 in Figure 3c,d, intercrystalline glass phases (glass phases) produced from the sintering additives Y_2O_3 and Al_2O_3 are analyzed.

Figure 4a shows the Vickers hardness of the samples SN and SNZ at elevated temperatures of 25°C, 300°C, 600°C, and 900°C in Ar. It is easy to understand that with the increase in temperatures, the hardness of ceramics decreases gradually, and for sample SN, its hardness

Element (wt. %)	Spectrum 1	Spectrum 2	Spectrum 3
Si	2.12	36.14	35.24
C	20.52	19.86	20.23
N	7.99	14.87	13.07
O	2.96	17.28	17.06
Al	~	3.31	3.54
Y	~	8.53	10.85
Zr	66.40	~	~

* All results in weight%.
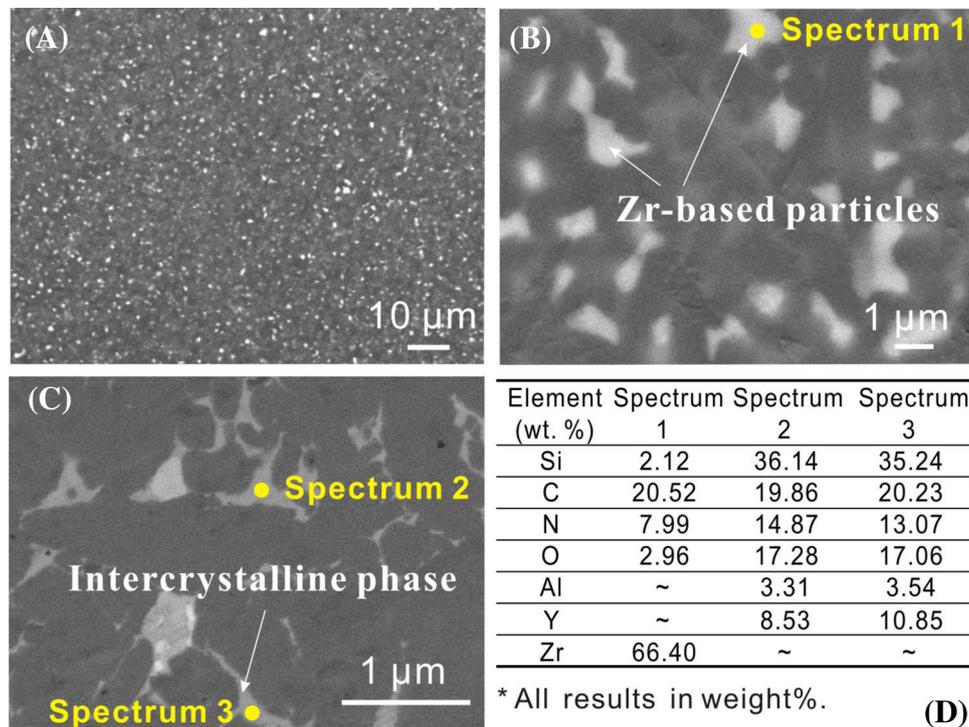
FIGURE 3 (a) Backscattered scanning electron microscopy (BSE-SEM) images of the Zr-containing Si_3N_4-based composite, and the local areas are magnified in (b) and (c). (d) Energy-dispersive X-ray spectroscopy (EDS) point analysis.
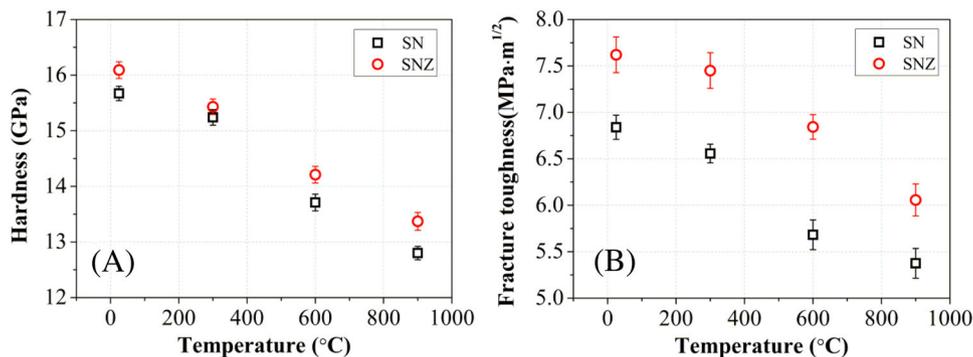
FIGURE 4 (a) Vickers hardness and (b) fracture toughness of samples Si_3N_4 (SN) and Zr-containing Si_3N_4 (SNZ) at elevated temperatures of 25°C, 300°C, 600°C, and 900°C.

value reduces from 15.7 GPa at 25°C to 12.8 GPa at 900°C. In contrast, the sample SNZ presents increased Vickers hardness in the whole temperature range when compared to sample SN, which is attributed to the load support of the hard phase ZrN.[38] It should be noted that for Si_3N_4 sample with direct ZrO_2 addition, its hardness at room temperature is 15.0 GPa, which is slightly lower than that of monolithic Si_3N_4. It is shown that the incorporation of ZrO_2 worsens the hardness of ceramics. Similar to Vickers hardness, although the fracture toughness of ceramics deteriorates with temperature, the existence of Zr-based particles is effective for enhancing the fracture toughness of Si_3N_4, and the toughness values of sample SNZ at 25°C

and 900°C are 7.6 and 6.1 $MPa \cdot m^{1/2}$, which are 11% and 13% higher than that of sample SN, respectively. In addition, as shown in Table 1, the mechanical properties of the $Si_3N_4/ZrN/ZrO_2$ composite at room temperature are compared with those of the Si_3N_4 reference samples. The obtained ceramic maintains a reasonable hardness and fracture toughness based on the formation of ZrN and ZrO_2.

To explore specific toughening mechanism, the indentation morphology is investigated in detail. As shown in Figure 5a, a pyramidal indentation after Vickers loading remains on the surface of sample SN, where the four cracks emerging from the corners extend out. By enlarging one of
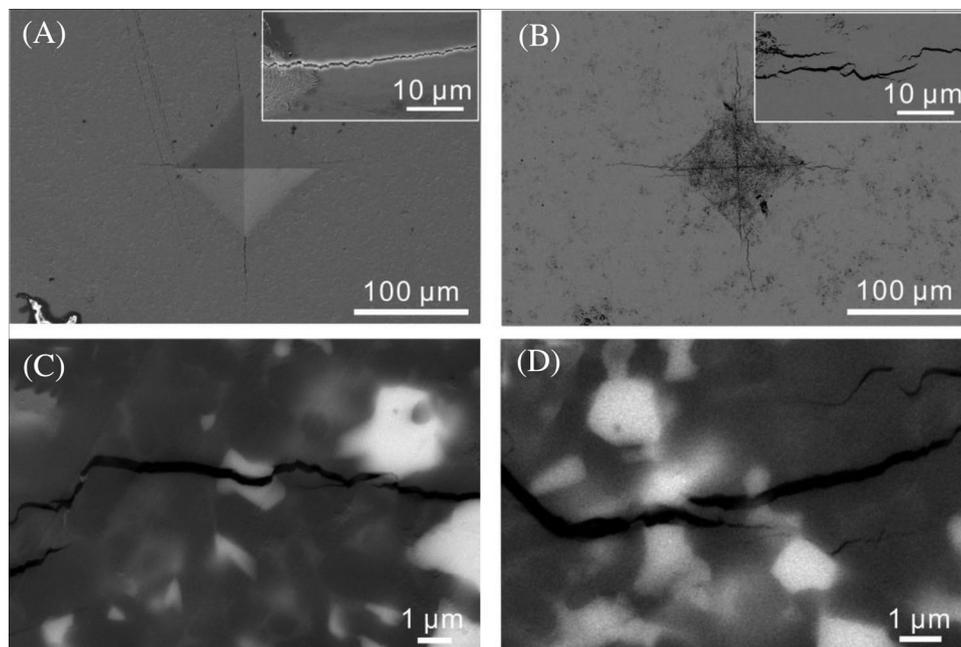
FIGURE 5 Vickers indentations of samples (a) Si_3N_4 (SN) and (b) Zr-containing Si_3N_4 (SNZ) at 25°C, and one corner of them is magnified in the insets. (c and d) Backscattered scanning electron microscopy (BSE-SEM) images of sample SNZ.

TABLE 1 Comparison of Vickers hardness and fracture toughness of the obtained composite with that of reported Si_3N_4-based ceramics at room temperature.

Samples	Vickers hardness (GPa)	Fracture toughness (MPa·m$^{1/2}$)	Reference
Si_3N_4/ZrO_2	13.2–14.5	6.1–7.1	[23]
Si_3N_4/HfB_2	20.4–21.5	3.5–7.7	[39]
Si_3N_4/ZrB_2	~20	~10	[40]
$Si_3N_4/FeSi_2$	~13.7	~9.8	[41]
Si_3N_4/TiN	~14	~5.9	[42]
Si_3N_4/TiC	16.1–17.3	7.7–8.4	[43]
$Si_3N_4/TiC_{0.3}N_{0.7}$	13.3–14.3	7.9–9.4	[11]
Si_3N_4/ZrN	~22.5	~6.2	[38]
$Si_3N_4/ZrN/ZrO_2$	~16.1	~7.6	This work

the corners (inset in Figure 5a), it is found that the crack path is straight without any branching, which is a typical crack pattern of brittle structural ceramics. In contrast, for sample SNZ, as shown in Figure 5b, the average horizontal length of the pyramidal indentation is less than that of sample SN, from ~70 to ~64 μm, and the crack track induced is diverse. In addition to the rugged path, more branches are evolved around the main crack, thus relieving the stress concentration at the crack tip and contributing to the enhanced fracture toughness of Si_3N_4. With the switching of scanning mode to backscattering, the role of Zr-based particles is highlighted. Figure 5c,d shows the

crack propagation of sample SNZ at 25°C. On the one hand, the Zr-based particle is divided into two halves in the process of crack advancing, namely, the transgranular fracture of particles (Figure 5c). On the other hand, the fine crack propagates along the grain boundary between the Si_3N_4 and Zr-based particles, resulting in the deflection and bridging of cracks (Figure 5d). As well known, transgranular and intergranular fractures are two common fracture modes of brittle ceramics, in which intergranular fracture contributes to enhanced toughness of ceramics as it relieves the stress concentration at the crack tip and thus consumes more fracture energy. Thus, the enhanced fracture toughness of the SNZ ceramic composite is discussed in terms of an intergranular fracture mode behavior.[44]

To reveal the high-temperature oxidation behavior of Si_3N_4-based composite, a series of oxidation experiments were carried out in the air at 1000°C, 1300°C, and 1500°C for 5 h. Figure 6a first records the weight gain per unit surface area (ΔW) of the studied samples. It is known that ΔW depends greatly on the heat-treatment temperature, and it shows an upward trend. At 1000°C, the ΔW of samples SN and SNZ is almost zero, reflecting the intrinsic oxidation resistance of Si_3N_4.[45,46] As the temperature increases, the oxidation of Si_3N_4 is gradually prominent. By comparison, the presence of Zr-based particles leads to a more violent oxidation behavior of Si_3N_4, and the ΔW of SNZ is always higher than that of SN. Figure 6b measures the sample's density after oxidation at different temperatures. Due to the incorporation of Zr, the density of SNZ is slightly higher than that of SN, and both densities are maintained at ~3.4
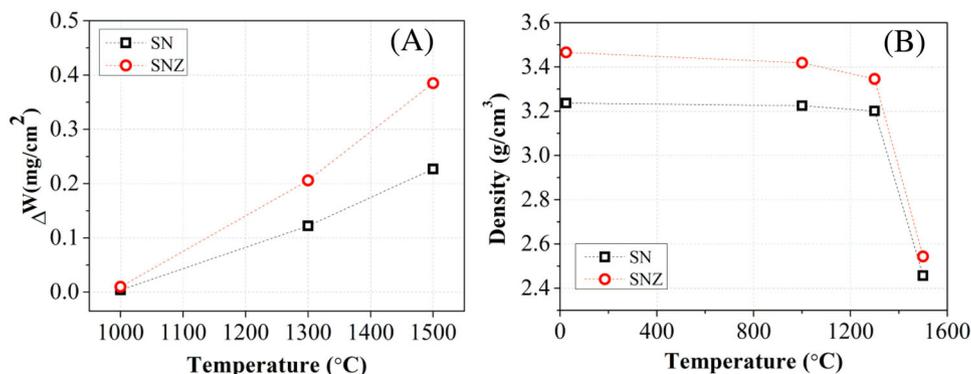
FIGURE 6 (a) Specific weight gains of samples Si_3N_4 (SN) and Zr-containing Si_3N_4 (SNZ) after oxidation at 1000°C, 1300°C, and 1500°C. (b) Density of the oxidized samples SN and SNZ.
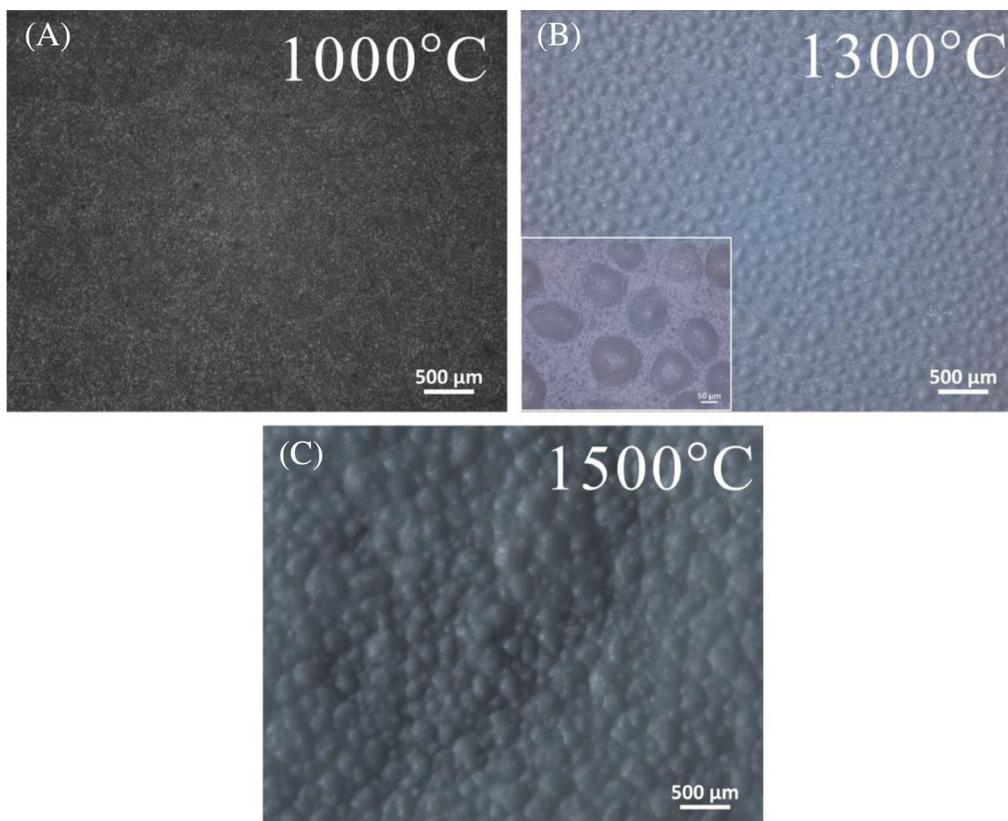
FIGURE 7 Optical images of surface morphologies of sample Zr-containing Si_3N_4 (SNZ) after oxidation at (a) 1000°C, (b) 1300°C, and (c) 1500°C.

and $\sim$3.2 g/cm^3 in the temperature range of 25°C–1300°C. As the temperature increases to 1500°C, the density of samples drops suddenly, and the specific reasons will be discussed later.

Figure 7 exhibits the optical images of the oxidation morphology of sample SNZ at 1000°C, 1300°C, and 1500°C. From Figure 7a, it can be seen that the ceramic surface is flat and smooth at 1000°C. However, a large number of bubbles appear on the oxidized surface at 1300°C, as

shown in Figure 7b. By enlarging the local area (inset in Figure 7b), these bubbles have a convex structure with a uniform size of $\sim$100 μm. When the oxidation temperature increases to 1500°C, the oxidation behavior is more intense. Accordingly, the bubbles become larger and thus result in a coarser surface morphology (Figure 7c). As a non-oxide ceramic, the passive oxidation occurs for Si_3N_4 at elevated temperatures,[47] and it reacts with sufficient oxygen to form SiO_2 oxide films according to Equation (3).
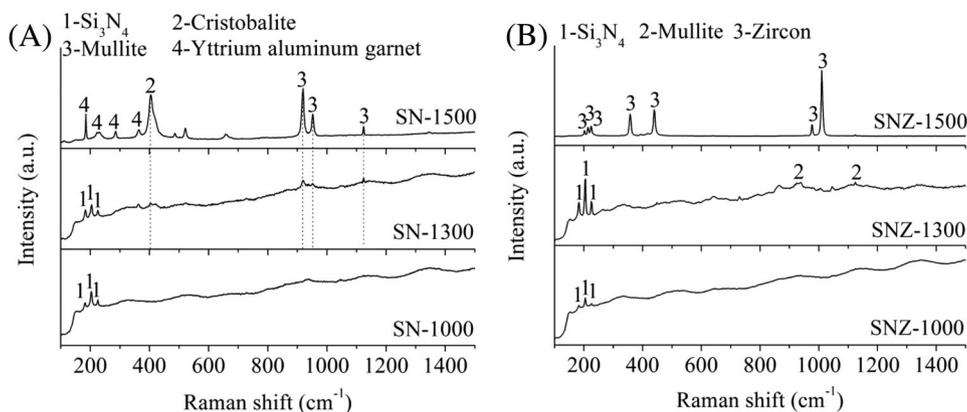
FIGURE 8 Raman spectra of samples (a) Si_3N_4 (SN) and (b) Zr-containing Si_3N_4 (SNZ) after oxidation at 1000°C, 1300°C, and 1500°C.

Herein, it can be speculated that the presence of bubbles is relevant to the release of N_2.[48]

$$Si_3N_{4(s)} + 3O_{2(g)} = 3SiO_{2(s)} + 2N_{2(g)} \quad (3)$$

Raman test is implemented to analyze the chemical composition of the oxide layers formed on the surface of the ceramics. Figure 8a shows the Raman spectra of sample SN at different temperatures (sample name plus corresponding numbers). It is obvious that at 1000°C and 1300°C Raman peaks in the spectra mainly consist of crystalline β-Si_3N_4, and only a small amount of oxidation products, for example, cristobalite and mullite are identified at 1300°C. As the temperature rises to 1500°C, the oxidation of Si_3N_4 intensifies, which reacts with atmospheric oxygen, thus leading to the formation of a "silicate" layer.[48] At this time, in addition to high amounts of cristobalite and mullite, the yttrium aluminum garnet (YAG) is found in the oxide layer, which suggests the diffusion of the intergranular phase from the matrix to ceramic surface.[49,50] For sample SNZ, there is no significant change in the chemical composition of the oxide layers at 1000°C and 1300°C (Figure 8b). It is worth noting that when the oxidation temperature reaches 1500°C, the formation of zircon ($ZrSiO_4$) is identified.[51] This result hints that the ZrO_2 in the matrix is transported through the "silicate" layer for reaction with SiO_2, resulting in the formation of $ZrSiO_4$.

To further clear the formed oxide layer, Figure 9 shows the XRD patterns of the samples SN and SNZ after annealing in air at 1500°C. After Rietveld refinement, it is seen from Figure 9a that for sample SN-1500 the oxide layer consists of SiO_2 (cristobalite), $Si_4Al_2O_{11}$ (aluminum silicate), and $Y_3Al_5O_{12}$ (garnet), which is in line with the above Raman analysis, thereby confirming the formation of "silicate" layer. In contrast, for sample SNZ-1500 the component of oxide layer is relatively simple, which is a mixture composition of SiO_2 (cristobalite) and $ZrSiO_4$

(Figure 9b). This result confirms the crystallization of $ZrSiO_4$ based on the chemical reaction between SiO_2 and ZrO_2 at high temperatures. It needs to be noted that there are some peaks that fail to identify in two patterns, such as the diffraction peaks located at ~30° and ~50° of sample SNZ-1500 and the exact composition of the oxide layer remains unresolved.

Figure 10 shows the cross-section of sample SNZ at 1300°C and 1500°C. From images, it is seen that Si_3N_4 matrix maintains high densification even if oxidized at 1500°C. Combined with EDS analysis (O mapping is inserted in Figure 10a), the formation of oxide layers on the surface of ceramics is demonstrated, in which yellow dashed lines are used to differentiate the Si_3N_4 matrix and oxide layer. From Figure 10a, it is seen that the thickness of the oxide layer is ~170 μm at 1300°C, while the layer thickness is widened to 0.66 mm as the temperature rises to 1500°C (Figure 10c). This result suggests that high temperature intensifies the oxidation of ceramics, leading to the growth of oxide layers. To illustrate the microstructure evolution, the local morphology of the oxide layers is magnified in Figure 10b,d. At 1300°C, although many fine pores appear in the oxide layer (Figure 10b), the oxide layer at this time is relatively dense and can fit well with the Si_3N_4 substrate (see Figure S2). In contrast, there is a great change in sample volume, when oxidized at 1500°C. As shown in Figure 10c, macroscopic pores are formed in the oxide layer. The existence of these pores is unfavorable to the impregnation of water molecules, thus resulting in a sudden decrease in the density of the samples (see Figure 6b). In addition, the microstructure of the oxide layer at 1500°C (Figure 10d) is relatively dense compared to that found at 1300°C. It is well known that $ZrSiO_4$ is an effective refractory material with excellent thermo-physical properties such as low thermal expansion, low thermal conductivity, as well as a good oxidation resistance.[52] Here, it can be inferred that the incorporation
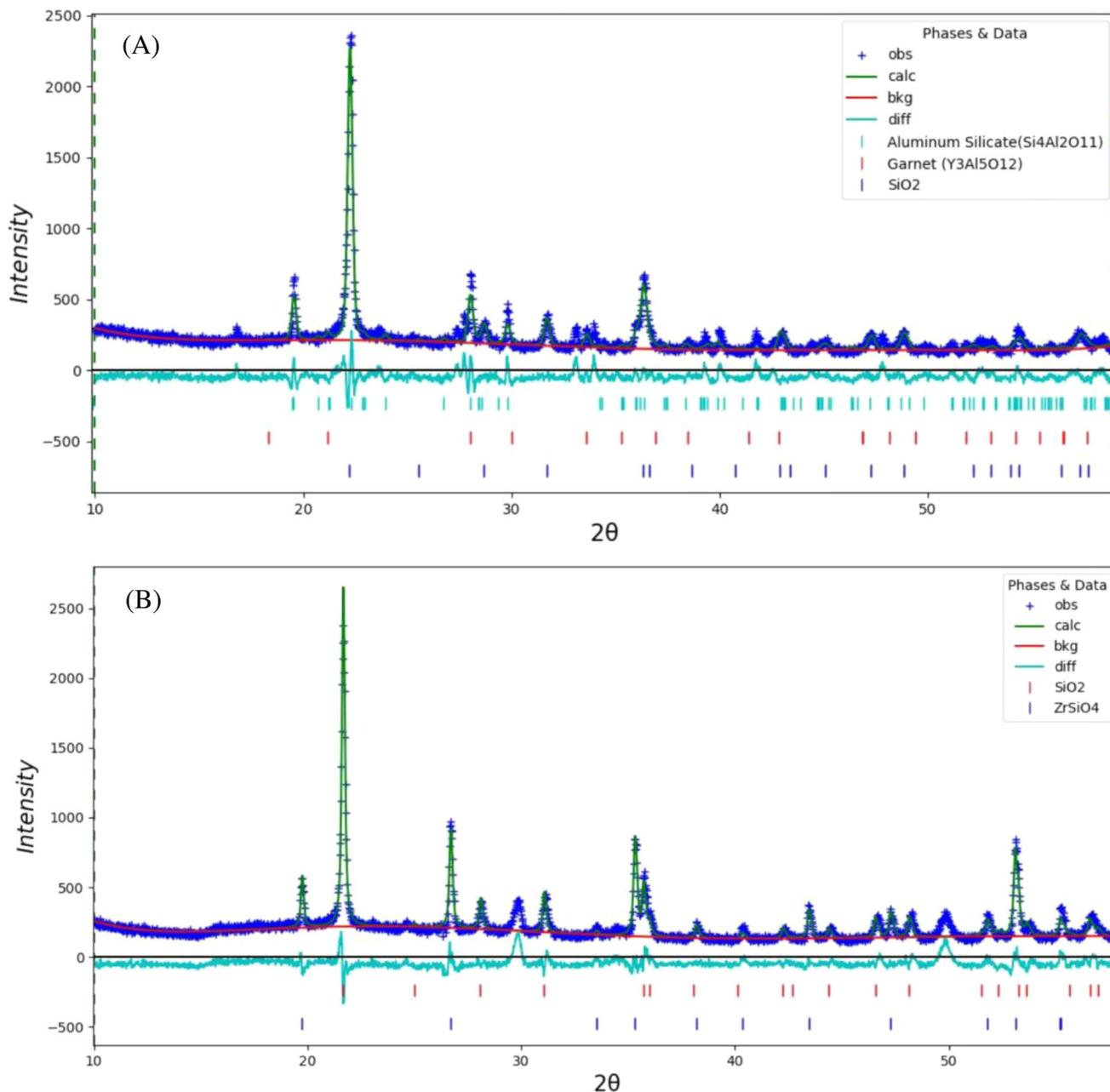
FIGURE 9   X-ray diffraction (XRD) patterns of samples (a) Si_3N_4 (SN) and (b) Zr-containing Si_3N_4 (SNZ) after oxidation at 1500°C.

of $ZrSiO_4$ is helpful to enhance the thermal and structural stability of the oxide layer.

Figure 11 shows the temperature-dependent thermal diffusivity of samples SN and SNZ after oxidation at 1000°C and 1300°C. Due to the rough oxidation surface, the thermal diffusion behavior for samples oxidized at 1500°C cannot be accurately recorded. The thermal diffusivity of all samples reduces as the temperature increases from 100°C to 1000°C. For instance, the thermal diffusivity of SNZ-1300 decreases from an initial value of 10.07 cm^2/s (at 100°C) to a final value of 3.64 cm^2/s (at 1000°C). Phonon–phonon scattering is the dominant scattering mechanism at high temperatures, and the temperature dependence of

thermal diffusivity shown in Figure 11 is thereby reasonable. At the same time, more information can be extracted from Figure 11: (i) In comparison to sample SN-1000, the formation of ZrO_2 and ZrN leads to higher values for the thermal diffusivity of the composite. In general, the presence of oxides is supposed to be one of the strategies to reduce the thermal diffusivity of Si_3N_4.[53] Here, the specific reasons that contribute to the increase of thermal diffusivity are still uncertain, which may be related to various microstructural factors (content of intergranular phases, and alignment of elongated Si_3N_4 grains) caused by the formed ZrO_2 and ZrN.[54–56] (ii) On the other hand, it can be found that whether sample SN-1300 or sample
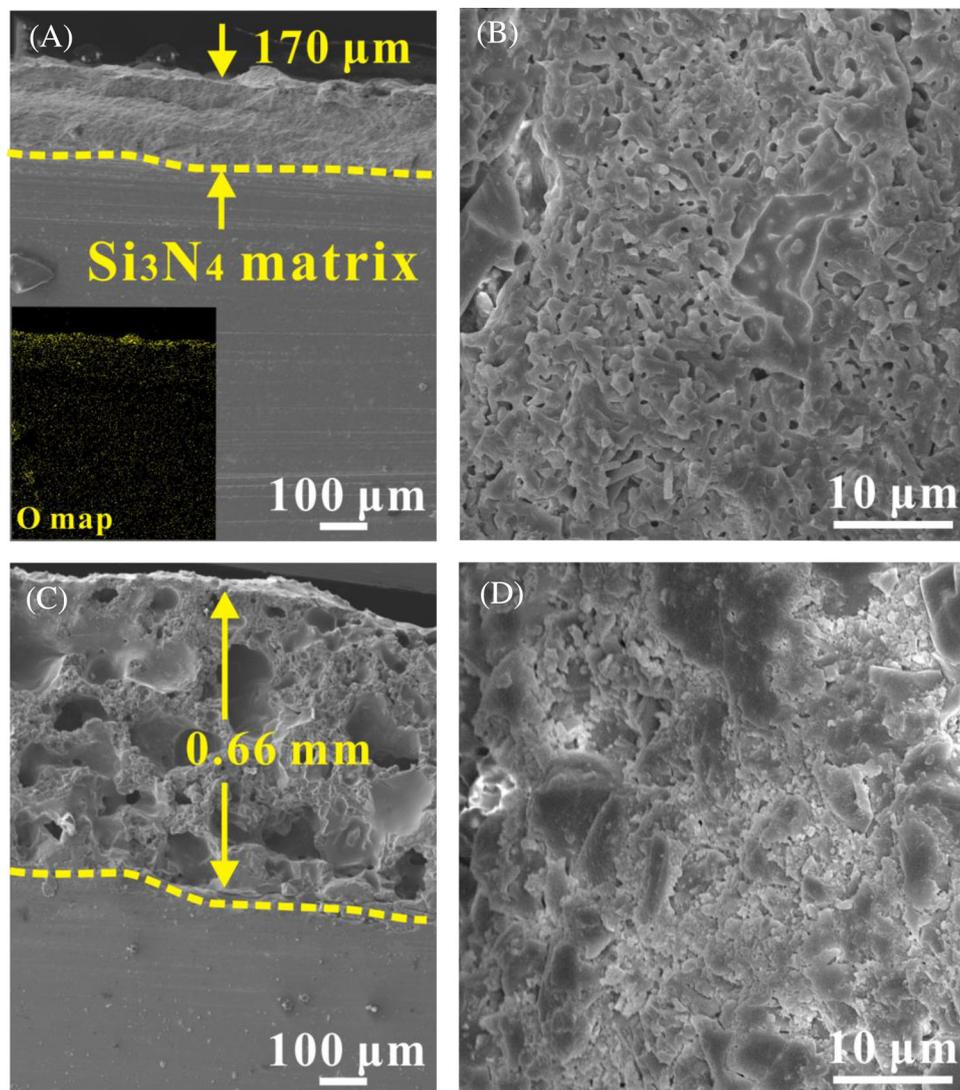
FIGURE 10 Scanning electron microscopy (SEM) images of cross-section of the Zr-containing Si_3N_4 (SNZ) sample after oxidation at (a) 1300°C and (c) 1500°C, and the corresponding local morphology of the oxide layers is enlarged in (b) and (d).

SNZ-1300 exhibits a high thermal diffusivity, compared to the samples SN-1000 and SN-1000 without formed oxide layer. In fact, in addition to the microstructural factors, the content of oxygen that is dissolved in the crystal lattice is crucial for the thermal properties of ceramics.[57,58] Hirao and coworkers[59] confirmed that the thermal conductivity of Si_3N_4 can be significantly improved by reducing the lattice oxygen content. In this work, Si_3N_4-based ceramics are sintered using Y_2O_3 and Al_2O_3 as sintering aids, which allows liquid-phase sintering via the formation of intergranular phases Y_2O_3–Al_2O_3. Accompanied by the start of oxidation, the intergranular phases gradually diffuse from the ceramic substrate to the surface (see Figures 7 and 10), which is possible to reduce the lattice oxygen content. In particular, as the oxidation temperature increases, the intensified oxidation behavior promotes the formation and growth of the oxide layer, thus triggering

the continuous consumption of lattice oxygen. Also, it is worth noting that because $ZrSiO_4$ is not formed at 1300°C, its effect on the thermal diffusivity of Si_3N_4 is negligible.

4 | CONCLUSIONS

This work focuses on high-temperature mechanical properties and oxidation behavior of the SNZ-based ceramic composite. Using $Zr(NO_3)_4$ as the additional phase, the Si_3N_4-based composite containing ZrO_2 and ZrN particles was fabricated during SPS at 1680°C. The in situ formed ZrO_2 and ZrN with a size of ~1 μm are uniformly dispersed in the Si_3N_4 matrix. Compared to monolithic Si_3N_4, the incorporation of Zr-based particles increases the Vickers hardness and fracture toughness of the composites at elevated temperatures of 25°C, 300°C, 600°C, and 900°C.
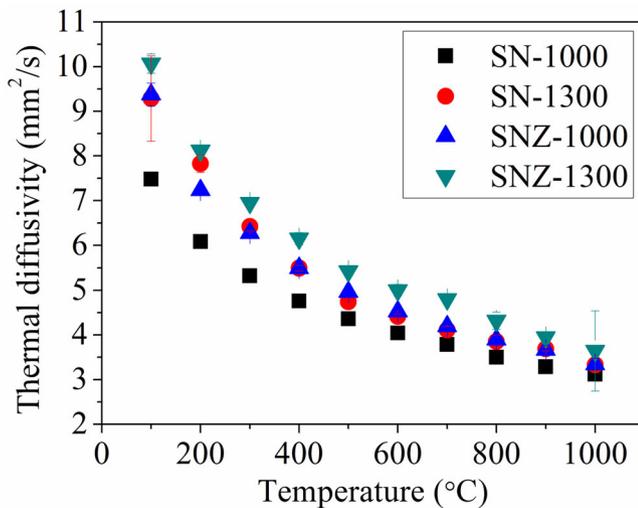
FIGURE 11 The temperature-dependent thermal diffusivity of oxidized samples Si_3N_4 (SN) and Zr-containing Si_3N_4 (SNZ) in the temperature range of 100°C–1000°C.

The reinforcing mechanism is on the one hand attributed to the load support of hard phase ZrN, on the other hand, it is a result of the crack deflection and bridging. The oxidation experiments revealed that Si_3N_4 experiences a passive oxidation, and the porous oxide layers are formed on the surface of ceramics at 1300°C, which gradually thickens as the temperature rises to 1500°C. For monolithic Si_3N_4 the oxide layer at 1500°C is composed of silica, mullite, and YAG. Accompanied by the incorporation of Zr, the oxide layer is mixture of SiO_2 and $ZrSiO_4$. The formation of oxide layer leads to an increased thermal diffusivity of Si_3N_4-based composite. It is expected that the findings developed here can provide guidance for preparing advanced Si_3N_4 ceramics and expanding their applications at high temperatures.

ORCID

Jiongjie Liu https://orcid.org/0000-0002-9379-6962
Emmanuel Ricohermoso III https://orcid.org/0000-0002-4093-4751
Zhuihui Qiao https://orcid.org/0000-0002-3535-3119
Xingmin Liu https://orcid.org/0000-0001-6130-6618
Emanuel Ionescu https://orcid.org/0000-0002-3266-3031
Ralf Riedel https://orcid.org/0000-0001-6888-7208

REFERENCES

1. Sternitzke M. Structural ceramic nanocomposites. J Eur Ceram Soc. 1997;17(9):1061–82.
2. Rathod VT, Kumar JS, Jain A. Polymer and ceramic nanocomposites for aerospace applications. Appl Nanosci. 2017;7(8):519–48.
3. Zhu S, Cheng J, Qiao Z, Yang J. High temperature solid-lubricating materials: a review. Tribol Int. 2019;133:206–23.
4. Fu Y, Zhang Y, Chen H, Yin X, Zhang J, Sun J, et al. Ultra-high temperature resistance of one-dimensional hafnium carbide wrapped with pyrolytic carbon up to 2450°C. Corros Sci. 2022;195:110015.
5. Gasch MJ, Ellerby DT, Johnson SM. Ultra high temperature ceramic composites. Handbook of ceramic composites. Springer; 2005. p. 197–224.
6. Levine SR, Opila EJ, Halbig MC, Kiser JD, Singh M, Salem JA. Evaluation of ultra-high temperature ceramics for aeropropulsion use. J Eur Ceram Soc. 2002;22(14–15):2757–67.
7. Zhou Y, Hyuga H, Kusano D, Yoshizawa Y-I, Hirao K. A tough silicon nitride ceramic with high thermal conductivity. Adv Mater. 2011;23(39):4563–7.
8. Watari K. High thermal conductivity non-oxide ceramics. J Ceram Soc Jpn. 2001;109(1265):S7–16.
9. Skopp A, Woydt M, Habig K-H. Tribological behavior of silicon nitride materials under unlubricated sliding between 22°C and 1000°C. Wear. 1995;181:571–80.
10. Liu J, Wang Z, Yang J, Yin B, Sun Q, Liu Y, et al. Study on tribological behaviors of Si_3N_4 based ceramics sliding against POM under different solutions. Tribol Int. 2018;118:368–72.
11. Liu J, Yang J, Zhu S, Cheng J, Yu Y, Qiao Z, et al. Temperature-driven wear behavior of Si_3N_4-based ceramic reinforced by in situ formed $TiC_{0.3}N_{0.7}$ particles. J Am Ceram Soc. 2019;102(7):4333–43.
12. Sun Q, Yang J, Yin B, Tan H, Liu Y, Liu J, et al. Dry sliding wear behavior of β-sialon ceramics at wide range temperature from 25 to 800°C. J Eur Ceram Soc. 2017;37(15):4505–13.
13. Liu J, Yang J, Yi G, Ma J, Yu Y, Qiao Z, et al. Effect of high-temperature oxidation on Si_3N_4 containing Ti_3AlC_2. Ceram Int. 2020;46(10):14697–705.
14. Narushima T, Goto T, Hirai T, Iguchi Y. High-temperature oxidation of silicon carbide and silicon nitride. Mater Trans, JIM. 1997;38(10):821–35.
15. Ohnabe H, Masaki S, Onozuka M, Miyahara K, Sasa T. Potential application of ceramic matrix composites to aero-engine components. Composites Part A. 1999;30(4):489–96.
16. Cho J, Boccaccini AR, Shaffer MS. Ceramic matrix composites containing carbon nanotubes. J Mater Sci. 2009;44(8):1934–51.
17. Wang L, Qi Q, Yang X, Zhang H, Liu Z, Ge S, et al. Mechanical properties optimization of Si_3N_4 ceramics by in-situ introduction of core–shell structural W-Fe_5Si_3. Compos B Eng. 2020;196:108134.

18. Balázsi C, Fényi B, Hegman N, Kövér Z, Wéber F, Vértesy Z, et al. Development of CNT/Si_3N_4 composites with improved mechanical and electrical properties. Compos B Eng. 2006;37(6):418–24.

19. Feng B, Fetzer AK, Ulrich AS, Galetz MC, Kleebe HJ, Ionescu E. Monolithic ZrB_2-based UHTC s using polymer-derived Si(Zr, B)CN as sintering aid. J Am Ceram Soc. 2022;105(1):99–110.

20. Feng B, Peter J, Fasel C, Wen Q, Zhang Y, Kleebe HJ, et al. High-temperature phase and microstructure evolution of polymer-derived SiZrCN and SiZrBCN ceramic nanocomposites. J Am Ceram Soc. 2020;103(12):7001–13.

21. Harrison R, Lee W. Processing and properties of ZrC, ZrN and ZrCN ceramics: a review. Adv Appl Ceram. 2016;115(5):294–307.

22. Guo WM, Wu LX, Yu JJ, Zeng LY, Sun SK, Li JX, et al. Effect of ZrB_2 content on phase assemblage and mechanical properties of Si_3N_4–ZrB_2 ceramics prepared at low temperature. J Am Ceram Soc. 2018;101(11):4870–5.

23. Sayyadi-Shahraki A, Rafiaei SM, Ghadami S, Nekouee KA. Densification and mechanical properties of spark plasma sintered Si_3N_4/ZrO_2 nano-composites. J Alloys Compd. 2019;776:798–806.

24. Talmy IG, Zaykoski JA, Opeka MM. High-temperature chemistry and oxidation of ZrB_2 ceramics containing SiC, Si_3N_4, Ta_5Si_3, and $TaSi_2$. J Am Ceram Soc. 2008;91(7):2250–7.

25. Diaz OG, Luna GG, Liao Z, Axinte D. The new challenges of machining ceramic matrix composites (CMCs): review of surface integrity. Int J Mach Tools Manuf. 2019;139:24–36.

26. Zapata-Solvas E, Gómez-García D, Domínguez-Rodríguez A. Towards physical properties tailoring of carbon nanotubes-reinforced ceramic matrix composites. J Eur Ceram Soc. 2012;32(12):3001–20.

27. Dai Q, Huang W, Wang X, Khonsari M. Directional interfacial motion of liquids: fundamentals, evaluations, and manipulation strategies. Tribol Int. 2021;154:106749.

28. Liu Y, Cheng L, Zhang L, Hua Y, Yang W. Microstructure and properties of particle reinforced silicon carbide and silicon nitride ceramic matrix composites prepared by chemical vapor infiltration. Mater Sci Eng A. 2008;475(1–2):217–23.

29. Reynaud P. Cyclic fatigue of ceramic–matrix composites at ambient and elevated temperatures. Compos Sci Technol. 1996;56(7):809–14.

30. Sørensen BF, Talreja R. Effects of nonuniformity of fiber distribution on thermally-induced residual stresses and cracking in ceramic matrix composites. Mech Mater. 1993;16(4):351–63.

31. Fan X, Ma X, Dang X, Xue J, Ye F, Zhao D, et al. In-plane thermal expansion behavior of dense ceramic matrix composites containing SiBC matrix. J Eur Ceram Soc. 2020;40(9):3414–22.

32. Liu J, Wang Z, Yin B, Yang J, Sun Q, Liu Y, et al. A novel method to prepare self-lubricity of Si_3N_4/Ag composite: microstructure, mechanical and tribological properties. J Am Ceram Soc. 2018;101(9):3745–8.

33. Liu J, Yang J, Yu Y, Sun Q, Qiao Z, Liu W. Self-lubricating Si_3N_4-based composites toughened by in situ formation of silver. Ceram Int. 2018;44(12):14327–34.

34. Evans AG, Charles EA. Fracture toughness determinations by indentation. J Am Ceram Soc. 1976;59(7–8):371–2.

35. Batha HD, Whitney ED. Kinetics and mechanism of the thermal decomposition of Si_3N_4. J Am Ceram Soc. 1973;56(7):365–9.

36. Salavati-Niasari M, Dadkhah M, Davar F. Synthesis and characterization of pure cubic zirconium oxide nanocrystals by decomposition of bis-aqua, tris-acetylacetonato zirconium (IV) nitrate as new precursor complex. Inorg Chim Acta. 2009;362(11):3969–74.

37. Stoia M, Barvinschi P, Barbu-Tudoran L, Negrea A, Barvinschi F. Influence of thermal treatment on the formation of zirconia nanostructured powder by thermal decomposition of different precursors. J Cryst Growth. 2013;381:93–9.

38. Zgalat-Lozynskyy O, Kud I, Ieremenko L, Krushynska L, Zyatkevych D, Grinkevych K, et al. Synthesis and spark plasma sintering of Si_3N_4–ZrN self-healing composites. J Eur Ceram Soc. 2022;42(7):3192–203.

39. Luo SC, Guo WM, Plucknett K, Lin HT. Improved toughness of spark-plasma-sintered Si_3N_4 ceramics by adding HfB_2. Ceram Int. 2021;47(6):8717–21.

40. Wu LX, Guo WM, Li JX, Wu SH, Lin HT. Si_3N_4–ZrB_2 ceramics prepared at low temperature with improved mechanical properties. J Eur Ceram Soc. 2017;37(13):4217–21.

41. Wang L, Qi Q, Cai P, Zhang H, Yang X, Liu X, et al. New route to improve the fracture toughness and flexural strength of Si_3N_4 ceramics by adding $FeSi_2$. Scr Mater. 2017;126(Suppl C):11–4.

42. Gao L, Li J, Kusunose T, Niihara K. Preparation and properties of TiN–Si_3N_4 composites. J Eur Ceram Soc. 2004;24(2):381–6.

43. Ye C, Yue X, Ru H, Long H, Gong X. Effect of addition of micronsized TiC particles on mechanical properties of Si_3N_4 matrix composites. J Alloys Compd. 2017;709:165–71.

44. Ohji T, Jeong YK, Choa YH, Niihara K. Strengthening and toughening mechanisms of ceramic nanocomposites. J Am Ceram Soc. 1998;81(6):1453–60.

45. Houjou K, Ando K, Liu S-P, Sato S. Crack-healing and oxidation behavior of silicon nitride ceramics. J Eur Ceram Soc. 2004;24(8):2329–38.

46. Tatarko P, Kašiarová M, Dusza J, Šajgalík P. Influence of rare-earth oxide additives on the oxidation resistance of Si_3N_4–SiC nanocomposites. J Eur Ceram Soc. 2013;33(12):2259–68.

47. Tripp W, Graham H. Oxidation of Si_3N_4 in the range 1300°C to 1500°C. J Am Ceram Soc. 1976;59(9–10):399–403.

48. Lewis M, Barnard P. Oxidation mechanisms in Si–Al–ON ceramics. J Mater Sci. 1980;15(2):443–8.

49. Falk L, Dunlop G. Crystallization of the glassy phase in an Si_3N_4 material by post-sintering heat treatments. J Mater Sci. 1987;22(12):4369–76.

50. Lewis MH, Bhatti A, Lumby RJ, North B. The microstructure of sintered Si–Al–ON ceramics. J Mater Sci. 1980;15(1):103–13.

51. Syme R, Lockwood D, Kerr H. Raman spectrum of synthetic zircon ($ZrSiO_4$) and thorite ($ThSiO_4$). J Phys C: Solid State Phys. 1977;10(8):1335.

52. Kaiser A, Lobert M, Telle R. Thermal stability of zircon ($ZrSiO_4$). J Eur Ceram Soc. 2008;28(11):2199–211.

53. Wang W, Yao D, Liang H, Xia Y, Zuo K, Yin J, et al. Effect of the binary nonoxide additives on the densification behavior and thermal conductivity of Si_3N_4 ceramics. J Am Ceram Soc. 2020;103(10):5891–9.

54. Yokota H, Ibukiyama M. Microstructure tailoring for high thermal conductivity of β-Si_3N_4 ceramics. J Am Ceram Soc. 2003;86(1):197–9.

55. Kitayama M, Hirao K, Toriyama M, Kanzaki S. Thermal conductivity of β-Si$_3$N$_4$: I, effects of various microstructural factors. J Am Ceram Soc. 1999;82(11):3105–12.

56. Ziegler G, Hasselman D. Effect of phase composition and microstructure on the thermal diffusivity of silicon nitride. J Mater Sci. 1981;16(2):495–503.

57. Virkar AV, Jackson TB, Cutler RA. Thermodynamic and kinetic effects of oxygen removal on the thermal conductivity of aluminum nitride. J Am Ceram Soc. 1989;72(11):2031–42.

58. Buhr H, Müller G, Wiggers H, Aldinger F, Foley P, Roosen A. Phase composition, oxygen content, and thermal conductivity of AIN (Y$_2$O$_3$) ceramics. J Am Ceram Soc. 1991;74(4):718–23.

59. Kitayama M, Hirao K, Tsuge A, Watari K, Toriyama M, Kanzaki S. Thermal conductivity of β-Si$_3$N$_4$: II, effect of lattice oxygen. J Am Ceram Soc. 2000;83(8):1985–92.

SUPPORTING INFORMATION

Additional supporting information can be found online in the Supporting Information section at the end of this article.